

promoting access to White Rose research papers



Universities of Leeds, Sheffield and York
<http://eprints.whiterose.ac.uk/>

This is an author produced version of a paper published in **Physical Review B: Condensed Matter and Materials Physics**.

White Rose Research Online URL for this paper:

<http://eprints.whiterose.ac.uk/77085/>

Paper:

Hardcastle, TP, Seabourne, CR, Zan, R, Brydson, RMD, Bangert, U, Ramasse, QM, Novoselov, K and Scott, AJ (2013) *Mobile metal adatoms on single layer, bilayer and trilayer graphene: an ab initio study correlated with experimental electron microscopy data*. Physical Review B: Condensed Matter and Materials Physics, 87 (19). 195430.

<http://dx.doi.org/10.1103/PhysRevB.87.195430>

Mobile metal adatoms on single layer, bilayer and trilayer graphene: an *ab-initio* DFT study with van der Waals corrections correlated with electron microscopy data

T. P. Hardcastle¹, C. R. Seabourne¹, R. Zan^{2,3}, R. M. D. Brydson¹, U. Bangert², Q. M. Ramasse⁴, K. S. Novoselov³ and A. J. Scott¹.

¹*Institute for Materials Research, SPEME, University of Leeds, Leeds LS2 9JT, UK*

²*School of Materials, University of Manchester, Manchester, M13 9PL, UK*

³*School of Physics and Astronomy, University of Manchester, Manchester, M13 9PL, UK*

⁴*SuperSTEM Laboratory, STFC Daresbury Campus, Daresbury, WA4 4AD, UK*

The plane-wave density functional theory code CASTEP was used with the Tkatchenko-Scheffler van der Waals correction scheme and the GGA PBE functional to calculate the binding energy of Au, Cr and Al atoms on the armchair and zigzag edge binding sites of monolayer graphene, and at the high-symmetry adsorption sites of single layer, bilayer and trilayer graphene. All edge site binding energies were found to be substantially higher than the adsorption energies for all metals. The adatom migration activation barriers for the lowest energy migration paths on pristine monolayer, bilayer and trilayer graphene were then calculated and found to be smaller than or within an order of magnitude of $k_B T$ at room temperature, implying very high mobility for all adatoms studied. This suggests that metal atoms evaporated onto graphene samples quickly migrate across the lattice and bind to the energetically favourable edge sites before being characterised in the microscope. We then prove this notion for Al and Au on graphene with scanning transmission electron microscopy (STEM) images showing that these atoms are observed exclusively at edge sites, and also hydrocarbon-contaminated regions, where the pristine regions of the lattice are completely devoid of adatoms. Additionally, we review the issue of fixing selected atomic positions during geometry optimisation calculations for graphene/adatom systems and suggest a guiding principle for future studies.

I. INTRODUCTION

A. Overview of recent theoretical studies of graphene-metal systems

The original synthesis of graphene¹ has subsequently sparked worldwide attention owing to its potential to revolutionise many areas of industry. Nanoelectronics is one such promising area, in which interfacing graphene via metal adatom/cluster contacts is a recurring theme²⁻⁸. This area of research is still developing and the consequences of particular dopants on the electronic properties of graphene are still being investigated. Widespread implementation of graphene-based electronics will therefore involve developing a more detailed understanding of metal-graphene interactions on a fundamental level. To this end, many theoretical studies using density functional theory (DFT) have already emerged which present predictions of binding energies and relaxed structures of various metal adatoms and clusters on pristine single layer graphene⁹⁻²⁴ and on graphene defect structures²⁵⁻³¹. Potential contacting applications will depend very much on the metal used because vacancy formation energies can be greatly reduced by certain dopants. In 2010, Karuoi et al.³¹ predicted that a Ni substrate assists graphene in healing its vacancy defects. In contrast, Boukhvalov and Katsnelson²⁶ predicted in 2009 that Fe, Ni and Co adatoms dramatically reduce vacancy formation energies in graphene, destroying it in the process. In this latter study Au atoms were predicted to have almost no effect on graphene vacancy formation energies, thus preserving its strength. We recently observed nanoscale holes being etched into pristine regions of graphene by various metal adatoms, with the exception of Au for which no etching process was seen to occur³².

Trends have emerged regarding the preferred binding sites for metal adatoms on graphene at absolute zero. Recent DFT studies^{11,14-16} predict that transition metals generally adsorb at the hollow (H) site (see Figure 3). Au atoms have been predicted to adsorb preferentially to the atop (A) site^{11,16,17}. It can be easy to erroneously conclude from these studies that one would expect stable and static configurations for these adatoms to exist on the basis of the local energetic minima predicted by geometry optimisation calculations at absolute zero. However, the calculated absolute difference in binding energy between adsorption sites is often very small, so it is sensible to suggest from these studies alone that the activation barriers for adatom migration are also small; small enough that the perturbing effects of room temperature, $T \sim 300$ K, cause certain metal adatoms to be highly mobile on graphene at room temperature^{14,16,29}.

DFT-calculated adatom binding energies are very sensitive to the exchange correlation functional used. To illustrate this, Table 1 shows binding energies of a single Au adatom on pristine single layer graphene taken from some recent *ab-initio* DFT studies^{9,10,12,17,18,25}. The local density approximation (LDA) functional is well known to significantly overbind compared to the generalised gradient approximation as parametrised by Perdew, Burke and Ernzerhof³⁶ (GGA PBE). This is evident from the values shown in Table 1. Despite the widespread success of the GGA PBE functional, it fails to accurately simulate non-local correlation effects which dominate in many biological and chemical systems. These systems are characterised by weak long-ranged interactions between instantaneous multipoles occurring in the electron density, collectively and commonly

referred to as van der Waals forces. The GGA PBE functional also fails to simulate interlayer interactions in graphite and multilayer graphene, thereby making non-corrected GGA functionals inappropriate for modelling involving structural relaxation of the systems in this paper. GGA-type van der Waals correction schemes for implementation into DFT codes have been designed by Grimme³⁷, Dion and Rydberg³⁸⁻⁴⁰, Jurečka et al.⁴¹ and Tkatchenko and Scheffler⁴² (TS). These correction schemes allow for new insight to be gained into possible surface physisorption bonding mechanisms between graphene and metal adatoms; an effect which is impossible to probe with the native LDA and GGA PBE functionals employed in virtually all DFT studies so far published. Moreover, van der Waals-corrected DFT sheds light on the graphene-metal interaction, not least because physisorption may be involved, but also because many laboratory synthesis methods produce samples containing regions which are multilayered^{32-35,43-46} and are therefore graphitic in character. To our knowledge, only two *ab-initio* DFT studies, by Amft et al.¹⁸ and Ming et al.⁴⁷, have incorporated non-local correlation effects with graphene/graphite-metal adatom systems. Amft et al.¹⁸ used the GGA-type correction schemes of Grimme³⁷ and Dion and Rydberg³⁸⁻⁴⁰ on single layer graphene/metal systems, and their values shown here in Table 1 aptly demonstrate the drastic effect of including these interactions.

B. Electron microscopy studies of graphene-metal systems

Whilst theoretical studies of graphene-metal systems are ubiquitous, a significant experimental insight of this system has recently emerged from a series of images obtained by our group³²⁻³⁵ using aberration-corrected scanning transmission electron microscopy (AC STEM) at 60 keV, examples of which are presented in Figure 1. In these studies, high angle annular dark field (HAADF) imaging was used to produce images which clearly showed suspended monolayer graphene membranes consisting of pristine regions along with defective and hydrocarbon-contaminated regions, onto which various metal adatoms had been evaporated. As Figure 1 shows, Au and Al atoms are observed exclusively at edge sites on the perimeters of etched holes or are clustered at hydrocarbon-contaminated regions. No metal adatoms were ever observed on these samples. A sample of variable thickness consisting of monolayer and multilayer regions and evaporated with Au was also prepared. By following the method of Eberlein et al.⁴⁸, electron energy loss spectra (EELS) were used to identify the monolayer, bilayer and trilayer regions unambiguously for this sample. The remaining regions were collectively identified as consisting of 4 or more layers. A very small number of isolated Au adatoms were found momentarily on the pristine regions of this sample, but only on areas whose thickness could be unambiguously identified as 4 or more layers. By using the approximate proportionality of the image intensity to the square of the atomic number, Z , the adsorption positions of these Au adatoms were determined, and found to be consistently at atop sites. In these studies we speculated that the graphene-metal binding energy may be significantly higher for thicker samples on account of the van der Waals-type contribution from the sublayers. We also speculated that all metal adatoms were very mobile on all of our samples and had migrated to defective and contaminated regions, presumed to be more stable, before the samples were characterised in the microscope.

Thus, the first aim of this paper is to use van der Waals-corrected DFT to predict the binding energy of selected metal adatoms at the high symmetry sites of pristine regions of graphene, and at the most commonly observed monolayer edge defects, in order to compare the energetic stability of these regions. The second aim is then to investigate adatom mobility on the pristine substrates by directly sampling the energy landscape corresponding to intermediate configurations between high symmetry adsorption sites in order to locate the transition state saddle points and thus evaluate the migration activation barriers. The van der Waals corrections will produce explicit and original evidence of how adatom binding energy and mobility changes with increasing graphene substrate thickness, if at all. To our knowledge, this is the first DFT study of a multilayer graphene-metal interaction to make a direct comparison with STEM data, the first study to calculate adatom migration barriers on both monolayer and multilayer graphene (real STEM specimens consist of multilayer regions in addition to single layers), and also the first such study to incorporate the van der Waals correction scheme of Tkatchenko and Scheffler⁴². In addition, we also address the apparent lack of agreement in the fixing of atomic positions during geometry optimisation calculations, a discussion of which now follows.

C. Discussion on long-ranged adatom-induced lattice perturbations and the constraining of atomic positions during geometry optimisation

The essence of the approximation with graphene adsorption studies is attempting to simulate the asymptotic flatness and stiffness of graphene far from the adsorbate, whilst accounting for the fact that adsorbate-induced lattice perturbations can be long-ranged, all under the constraints of finite supercell sizes dictated by the efficient use of shared computing architectures. (Real graphene is known to have ripples under typical laboratory conditions^{49,50}, but we neglect these effects here as the period of these oscillations is relatively large.) Lambin et al.⁵¹ recently demonstrated that for the case of N substitutional dopants in graphene with the LDA functional, the calculated local density of states differs significantly for 9×9 and 10×10 supercells. Although

adatom-induced lattice perturbations are likely to be smaller than those of substitutional dopants, the convergence of adatom binding energy should ideally be tested with supercell size, or the error due to the use of finite supercell sizes should at least be estimated. We carried out some tests using the LDA functional with 4×4 supercells with Au and Cr adatoms placed in the centre, in which all carbon atoms were relaxed. We found out-of-plane lattice perturbations to be significant at the supercell boundaries far from the adatom in response to the localised puckering near the adatom. This raises the question of whether such undulating structures are a physically meaningful simulation of graphene at all. Also, there is no well-defined way of measuring the distance of the adsorbate above the graphene plane in these systems. Despite it being something of an artifice, we advocate that fixing the positions of selected carbon atoms far from the adatom is a pragmatic way to simulate the stiffness and flatness of pristine graphene far from the adsorbate, but only if the supercells used are large enough to account for lattice perturbations to a justifiable level of energy convergence.

Further on the issue of fixing atomic positions, there appears to be no general consensus on the issue of *which* atomic positions should be fixed. We take the opportunity now to list the conventions used in recently published studies to illustrate the disparity, and then suggest a simple guiding principle for future studies. In the study by Sargolzaei and Gudarzi¹³, the positions of the adatom and the first nearest-neighbour carbon atoms were relaxed, with all other carbon positions fixed. Ding et al.¹⁰ state that they allowed all atomic positions to relax in the direction normal to the graphene plane, but it is unclear whether they also allowed for in-plane relaxations. Tang et al.²⁵ allowed all atoms in the calculation to relax in all directions. Amft et al.¹⁸ appear to have used the still different method of fixing the positions of the adatom and the carbon atoms on the supercell perimeter, whilst all other carbon positions were allowed to relax. Nakada et al.¹⁴ used yet another method and allowed all atoms to relax except for just one carbon atom far from the adatom, with the adatom only allowed to relax in the z (vacuum) direction. Whilst these different choices may or may not result in negligible differences in calculated binding energies for a given supercell size, most of them can introduce the easily avoidable idiosyncrasy of breaking the symmetry of the system. This is illustrated in Figure 2 which shows a 32 atom graphene monolayer supercell and the atop adsorption site (A) indicated with a red cross in the centre of the supercell. The C atoms on the supercell perimeter are indicated in blue to signify that their positions are fixed, whilst all remaining C atoms indicated in black are allowed to relax. By fixing the atoms indicated, the lattice environment encountered along the directions \vec{r}_1 and \vec{r}_2 is not the same as that along the direction \vec{r}_3 , despite the fact that these three directions are all supposed to be crystallographically equivalent. In fact, the resulting sublattices consisting of fixed and unfixed C atoms each have 2-fold rotational symmetry about the adsorption site as shown in Figure 2 (b) and (c), in contradiction with the 3-fold rotational symmetry of the complete lattice about the adsorption site. To restore the symmetry and create an environment for the adatom which is unbiased, we select C atoms to be fixed in our supercells so that i) C atoms which are fixed form a sublattice which shares the rotational symmetry of the complete lattice about the axis passing through the adsorption site of interest and ii) all of the remaining unfixed C atoms form a sublattice which shares the rotational symmetry of the complete lattice about that same axis. This is illustrated in Figures 9 and 10 (Appendix).

D. Binding sites, binding energy, and electrostatic dipole corrections

For the pristine regions, we confine our attention to the high symmetry points lying at the vertices of the symmetry-reduced Wigner-Seitz cells of the single and multilayer systems as indicated in Figure 3 (a) and (b). For lattice edges, the boundaries separating irreducible regions of the “zigzag” and “armchair” edges indicated in Figure 3 (c) and (d) are considered for the monolayer case for each of the 3 metals tested. The binding energy E_b at site X - where X takes the value X = A, A₁, A₂, B, H for adsorption sites, or C₁, C₂, Z₁, Z₂ for edge defect sites as appropriate - is defined in the conventional way as the difference in enthalpy of the composite system supercell and that of the sum of the two isolated system supercells:

$$E_b(X) = E_{C+m}(X) - E_m - E_C \quad (1.1)$$

where E_{C+m} is the TS-corrected enthalpy of the geometry-optimised graphene / metal supercell and E_m and E_C are the TS-corrected enthalpies of the isolated metal and geometry-optimised graphene supercells respectively.

One subtle but essential physical ingredient which can interfere with adsorption calculations is that of electrostatic polarity under periodic boundary conditions (PBC). A well-known difficulty which dates back to classical electrostatics is that the polarisation of an ionic crystal can depend on the definition of the (neutral) bulk unit cell if no explicit reference is made to the surface conditions. This has been expressed with great clarity in the context of *ab-initio* calculations by Makov and Payne⁵². Under the constraints of PBC, the crystal is infinite so the surface is undefined. Thus, with no surface cell to cancel out the spurious potential produced from unphysical interactions between periodic images of multipole moments in neighbouring supercells, the dipole moment of a neutral polar system can depend on the location of the supercell boundaries, or equivalently, on the placement of the system within the supercell. This positional-dependence of the energy arises because of

electron density overlapping with the cell boundary in the direction of the polarity, thus making the total cell dipole sensitive to the placement of the system. Metal adatom-graphene systems, especially adsorption configurations, tend to be polar in the vacuum direction owing to the charge transfer associated with the metal-carbon bond. Hence, it is essential that the systems are placed in the centre of the vacuum slab far from the supercell boundary at each end of the vacuum so as to ensure that the charge density is zero across this boundary. Various dipole correction schemes and studies of the subject have been published⁵³⁻⁵⁹. In this work we use the self-consistent electrostatic dipole correction scheme of Neugebauer and Scheffler⁵³ as implemented in CASTEP⁶⁰ to ensure that our input files satisfy the condition of zero charge density at the extremities of the vacuum slab.

II. METHOD

A. Exchange correlation functional, basis set parameters, optimisation of isolated structures and energy/enthalpy convergence with cell dimensions

Two van der Waals-corrected cell-optimised geometry optimisation calculations were carried out on the bulk graphite unit cell using the plane wave density functional theory code CASTEP⁶⁰ with the GGA PBE functional³⁶, Vanderbilt ultrasoft pseudopotentials⁶¹ and a temporary hyperfine basis set. The TS van der Waals correction scheme⁴² as implemented in CASTEP^{60,62} was used for the first calculation and the Grimme scheme³⁷ for the second. The fully-optimised Grimme-corrected final interlayer spacing was found to be 3.27 Å (3 s.f.), whereas the TS-corrected interlayer spacing was found to be 3.32 Å (3 s.f.); considerably closer to the experimentally measured⁶³ value of 3.35 Å. TS-corrected GGA PBE zero point energy calculations were then carried out to numerically converge the binding energy of a series of small graphene-metal systems, akin to those shown in Figure 8 (d) (Appendix), with respect to the kinetic energy cutoff E_C and k point spacings s^i (where $i = 1,2,3$ denotes correspondence to the reciprocal lattice vector b_i). A regular Monkhorst-Pack⁶⁴ k points grid was used in all cases, and for all subsequent calculations. The k point spacings were converged independently along in-plane and out-of-plane directions to ensure that any subtle behaviour at the Dirac points was captured to a satisfactory level of precision. On the basis of these calculations, the kinetic energy cutoff E_C and k point spacings s^i were picked at values satisfying $E_C = 550$ eV and $s^i < 0.035$ Å⁻¹. The TS / Grimme bulk lattice parameter validation test just described was then repeated with this basis set and both correction schemes were verified to produce the same interlayer spacings as before. The TS correction scheme was then chosen along with the established basis set parameters $E_C = 550$ eV and $s^i < 0.035$ Å⁻¹ for all subsequent calculations in the paper. Following this, the monolayer, bilayer and trilayer graphene unit cells were fully thermodynamically optimised with respect to bond lengths, vacuum thicknesses and layer spacings individually in each case using geometry optimisation calculations. The energy of isolated metal atom supercells and the binding energy of composite graphene/metal systems were converged with increasing supercell size in order to determine the required supercell dimensions for each system studied in this work. An exhaustive technical account of this procedure is given in the Appendix.

B. Adsorption site and defect site binding energy calculations

For the adsorption sites, the 3 monolayer graphene supercells shown in Figure 9 (a) - (c) (Appendix) were built, and a metal atom of species $m = \text{Au}, \text{Al}, \text{Cr}$ was placed into the centre of each supercell at an initial distance of 2 Å above the graphene sheet, to make nine supercells. The positions of the carbon atoms indicated in blue were fixed along all directions, and the positions of the adatom and carbon atoms indicated in black were allowed to relax in all directions. 2 and 3 layer versions of the four types of multilayer supercells shown in Figure 10 (a) - (d) (Appendix) were then constructed in an identical fashion for each of the three metals $m = \text{Au}, \text{Al}, \text{Cr}$, to make 24 more supercells. The carbon atom positions were fixed in the multilayer cases by simply applying the reasoning used for the monolayer cases independently to each carbon layer. All lattice parameters were fixed at the values indicated in Figures 9 and 10 (Appendix). For the edge defect sites, 4 supercells like those shown in Figure 4 were used, one for each of the 4 edge sites, whose lattice parameters were all fixed, and in which all atomic positions were relaxed with the metal atom placed 2 Å from the nearest carbon atom(s). These were duplicated into 3 copies, one set for each metal, to make 12 supercells. To curtail the risk of any of these systems failing to relax into an energetic minimum as a consequence of initial high symmetry, all systems were created with $P1$ symmetry and all symmetry finders were disabled. In addition to this, each metal atom was then offset from its initial site by 0.01 Å in the x direction.

The plane wave DFT code CASTEP⁶⁰ was then used with the TS van der Waals correction implementation⁶² and Vanderbilt ultrasoft pseudopotentials⁶¹ to carry out spin-polarized geometry optimisation calculations for

each of these 45 supercells. Valence states incorporated were $2s^2 2p^2$ for C, $5d^{10} 6s^1$ for Au, $3s^2 3p^6 3d^5 4s^1$ for Cr and $3s^2 3p^1$ for Al. To satisfy the k-points spacings convergence criterion, $s^i < 0.035 \text{ \AA}^{-1}$, determined in section II. A., a regular and uniformly-weighted $3 \times 3 \times 2$ Monkhorst-Pack⁶⁴ grid of 9 k-points was used to sample the Brillouin zone for the migration supercells illustrated in Figure 5 and the adsorption supercells in Figures 9 and 10 (Appendix). For the edge binding supercells illustrated in Figure 4, a $1 \times 2 \times 2$ grid totalling 2 k-points was used. For each series of self-consistent field (SCF) cycles used for the electronic minimisation, the exit criterion was imposed that the change in total electron energy between successive SCF cycles be converged to within $5 \times 10^{-7} \text{ eV}$. For the geometry optimisation, the Broyden–Fletcher–Goldfarb–Shanno (BFGS) optimisation algorithm⁶⁵⁻⁶⁹ was used with the following three convergence criteria: i) that the maximum force on all atoms be less than 0.01 eV \AA^{-1} , ii) that the maximum change in position for all atoms between successive BFGS steps be less than $5 \times 10^{-4} \text{ \AA}$ and iii) that the maximum change in the total system enthalpy between successive BFGS steps be less than $5 \times 10^{-6} \text{ eV per atom}$. The final TS-corrected enthalpies of these relaxed structures were then recorded as the values of $E_{C+M}(X)$ for insertion into equation (1.1). The values E_M and E_C were then calculated for insertion into equation (1.1), and the following measures were taken to exploit k-point error cancellation. Firstly, to evaluate the quantities E_M , the 45 final relaxed structure files were duplicated, and the copies were imported back into our visualisation software. All of the carbon atoms were then deleted, leaving just the metal atom(s) left in its final position in each case, and a spin-polarized TS-corrected total energy calculation was then performed for each of these 45 isolated metal atoms to evaluate the quantity E_M for each supercell separately. To evaluate the quantities E_C in equation (1.1) for the adsorption energies, the spin-polarized TS-corrected isolated graphene energies were calculated using the initial input supercells (i.e. pre-geometry optimisation), from which the metal atom was deleted in each case. For the edge site binding energies, the isolated graphene edge structures were fully relaxed to obtain spin-polarized TS-corrected enthalpy values E_C . These values were substituted into equation (1.1) to give the relaxed structure binding energies $E_b(X)$, which are plotted in Figure 6.

In order to estimate the error in the final values of adsorption binding energies owing to adatom-induced lattice perturbations, the binding energies of three fully relaxed 8×8 supercells were calculated; one for each metal. The binding energies for Cr and Al agreed with those of the 5×5 supercells up to a maximum discrepancy of 0.024 eV and 0.018 eV respectively, with a slightly larger maximum discrepancy of 0.056 eV recorded for the case of Au. These tests confirmed that whilst the calculated binding energies were likely to be somewhat underestimated owing to the limited supercell sizes employed in this study, the lattice perturbations for the adatoms studied were not significant enough to have an overriding influence on the main conclusions. Though the various approaches in this paper are computationally expensive (using large supercells and detailed basis sets), their rigorous nature and thorough design is beyond routine, novel and necessary to minimise errors and correctly account for often small energy differences.

C. Adatom migration activation barriers

Using the adsorption binding energy results of the next section, the migration pathways $H \rightarrow B \rightarrow H$ on all substrates were identified as obvious candidates for initial guesses of the lowest energy adatom diffusion pathways for Cr and Al, along with the paths $A \rightarrow B \rightarrow A$ ($A_1 \rightarrow B \rightarrow A_2$) on the monolayer (multilayer) substrates for Au. These paths were nominated because they comprise sites which give the lowest combination of binding energies which can be joined by a path traversing the entire unit cell. The established linear/quadratic synchronous transit (LST/QST) scheme of Halgren and Lipscomb⁷⁰ for determining reaction pathways, as modified to include conjugate gradient refinements and generalised to include periodic systems by Govind et al.⁷¹ and implemented in CASTEP⁶⁰ was used to locate the transition state configurations and thus evaluate the adatom migration activation barriers associated with these paths. The reactant and product states were first obtained by carrying out ultrafine geometry optimisation calculations with the pertinent adatoms at the path endpoints as indicated for the supercells illustrated in Figure 5. The reaction trajectory joining these reactant and product states was initially guessed by using the LST interatomic distance interpolation scheme⁷⁰, and the midpoint of this trajectory was used as the intermediate state to define the initial three-point QST pathway. A series of conjugate gradient minimisations and QST cycles were carried out from this point to locate the energy saddle point until the root mean square (RMS) of all atomic forces were converged to within 0.05 eV \AA^{-1} . All other calculation input parameters were the same as in section II. B. The resulting energy barriers are tabulated in Table 3.

III. RESULTS AND DISCUSSION

A. Binding energies and metal-carbon bond distances at absolute zero from *ab-initio* data

All metal adatoms and edge atoms settled onto the sites they were initially placed into, confirming that local energy minima exist for all configurations studied. The calculated binding energies E_b corresponding to the fully optimised configurations are tabulated in Table 2 and plotted in Figure 6. Figure 7 shows total electron density slices for Au adsorbed onto monolayer and trilayer graphene, and bound to the monolayer edge sites C_1 , C_2 , Z_1 and Z_2 . For all adsorption states for all metals, structural perturbations to the graphene lattice were small, as Figure 7 shows for the case of Au. The adsorption bonding character is seen to be consistent with physisorption. The increased adsorption energy for the trilayer case is evident from the smaller Au-graphene surface distance and the increased electron density between the Au and the binding carbon atom. In contrast, the binding energies at monolayer edge sites are much higher than the adsorption energies in all cases, confirming that these defect sites are much more stable, consistent with our STEM observations. These results are clearly supported by Figure 7, which shows a substantial region of electron density in between the C and Au at the edge sites, which warrants interpretation as a substantially stronger covalent chemical bond.

In Table 2, three distances are tabulated for the adsorption calculations: i) the distance(s) along the binding direction(s) from the adatom to the nearest carbon atoms (1 for sites A, A_1 and A_2 , 2 for site B and 6 for site H) ii) the distance along the z direction from the adatom to the nearest carbon atom(s) and iii) the distance along the z axis from the adatom to the fixed carbon atoms of the top layer. The difference between the latter two of these three distances is equal to the amount by which the top graphene layer had puckered out-of-plane. These puckering distances are all small, indicating that all metal adatoms do little to interfere with the structural integrity of the lattice. The binding energies are seen to significantly increase for increasing layer numbers for all of the metals tested, adding credibility to the notion that the van der Waals interaction with the sublayers accounts for a significant proportion of the metal-graphene binding energy in real laboratory samples. For each and every adsorption site and metal studied, the energy difference between the 2 and 3 layer cases is smaller than the difference between the 1 and 2 layer cases. This certainly seems like an intuitive result and it suggests that the binding energy converges towards that of the bulk graphite (0001) surface as the thickness is increased beyond 3 layers. Further calculations for higher numbers of graphene layers could be carried out to predict the thickness required to recover the behaviour of the bulk graphite (0001) surface, although it may be wise to resort to using symmetry finders to make such calculations computationally efficient, depending on the scaling behaviour of the code used.

A further important conclusion of the results is that the absolute difference in binding energy between the A_1 , A_2 , B and H adsorption sites remains unchanged for the various studied thicknesses. This is evident from the energy trends in Figure 6, in which it can be seen that the 2 layer and 3 layer data points for a given metal are all approximately related by a rigid translation along the energy axis. So despite the proportional contribution of the sublayers to the total binding energy being very significant, the energetic ordering of the adsorption sites is actually predicted to be independent of the thickness. This indicates that at absolute zero, the short-range carbon-metal binding occurring on the top layer takes precedence over the van der Waals contribution from the sublayers, giving rise to static configurations for which the energetically favoured adsorption site is unchanged, irrespective of how thick the sample is.

B. Adatom mobility supported by *ab-initio* results and observed using STEM

Despite the prediction that stable configurations exist for all metals and sites at $0 K$, this is in contrast to our STEM observations³²⁻³⁵ at room temperature, $T \sim 300 K$. We now argue that our migration activation barrier calculations summarised in Table 3 strongly support the notion that thermal effects cause the adatoms to be mobile along in-plane directions. Room temperature corresponds to a fundamental temperature of $k_B T = 0.026 eV$ (3 d. p.), where k_B is the Boltzmann constant. The magnitude of the metal-carbon binding energy in all cases is much larger than $k_B T$ at room temperature, so an argument based on thermal bond breaking cannot be invoked to account for the continual absence of adatoms on clean regions. However, the migration activation barriers presented in Table 3 for the case of monolayer substrates at $0 K$ are well below $k_B T$ for Au and Cr at $T \sim 300 K$, indicating that these adatoms are likely to be extremely mobile on all the substrates studied at room temperature. For Al, the activation barriers are between 0.166 and 0.197 eV (3 d. p.), within one order of magnitude of $k_B T$. This suggests that Al adatoms are likely to migrate at a slower rate than Au and Cr, although the barrier is nonetheless trivially small. Our results predict that lattice edge sites would result in significantly stronger adatom binding than the pristine, clean regions of the lattice. This is demonstrated very clearly by our recent STEM observations presented in Figure 1. We note that one recent study⁷² used DFT to predict binding energies of Au atoms at different types of edge site to be between 3.1 eV and 6.4 eV, in good agreement with our values. Thus, we conclude that all adatoms in our samples had migrated across the clean regions of the

lattice into more stable defective or contaminated regions within a short timeframe as a result of the statistical inevitability associated with perturbing thermal effects at $T \sim 300$ K. This migration occurred because of the small adatom migration barriers for samples of all thicknesses.

C. Comments on possible effects of the electron beam in our samples

We need to also consider the effect of the STEM electron beam on our specimens. A very small number of Au atoms were observed by STEM on clean regions some time after deposition of the adatoms. Whilst our published STEM images confirm that the beam does little or nothing to affect the integrity of the graphene itself at 60 keV, it is necessary to rationalise the circumstances whereby single metals are observed on clean regions of graphene. In most instances, regardless of specimen thickness and the metal species, the adatoms exist as clusters at defected or hydrocarbon contaminated regions of the sample. This can be understood by the high mobility of the adatoms, and the greater energetic stability of adatom binding at these sites. We conjecture that in cases where Au atoms were observed by STEM on clean thicker regions³², the beam may have displaced these Au atoms from clusters in the more stable regions during the scanning process. Considerations based on a recent quantitative study of beam damage in graphene⁷³ could be used to test these remarks. This is not to suggest we do not recognise the possibility of knock-on damage in our microscopy experiments, local heating effects (which are arguably negligible⁷⁴) or the temporary localised accumulation of negative charge around the beam. These effects were not however explicitly considered in this study. In summary, we consider migration effects to be the pivotal reason why adatoms are not generally observed on clean graphene regions, with electron beam knock-on effects being a secondary consideration. Indeed, the beam itself is attributed as a possible reason for the observation of single Au atoms on clean regions due to displacement effects.

IV. CONCLUSIONS

We have presented DFT calculations for the binding energy of Au, Al and Cr atoms bound at graphene edge sites and adsorbed on monolayer, bilayer and trilayer graphene using the van der Waals-correction scheme of Tkatchenko and Scheffler⁴² for the first time. The contribution to the total binding energy from graphene sublayers was predicted to be very significant, although the edge binding energies were found to be substantially higher for all atoms in all cases. Migration activation barriers for these adatoms on monolayer, bilayer and trilayer graphene were then calculated and shown to be smaller than or within one order of magnitude of $k_B T$ at room temperature in all cases, implying that these adatoms are extremely mobile on graphene at room temperature. It was concluded from this that graphene samples doped with Au, Cr and Al should be seen to be completely devoid of these dopants on the pristine regions, with the dopants binding preferentially to the edge defect sites. This was shown to be in striking agreement with the STEM data presented in Figure 1 of this study, along with our recently published STEM observations³²⁻³⁵. Additionally, a brief review of atomic position fixing conventions adopted in recently published calculations was presented, and a simple guiding principle based on lattice symmetries was suggested for future studies.

V. APPENDIX

Optimisation of isolated structures and energy/enthalpy convergence with cell dimensions – Further Information

The single layer graphene unit cell shown in Figure 8 (a) was constructed, whose initial in-plane lattice vectors $\vec{a}_{11}^{(i)}$ and $\vec{b}_{11}^{(i)}$ were left unconstrained and both set initially at the experimentally-measured⁶³ bulk graphite value of 2.461 Å. This unit cell was then duplicated, and the vacuum-direction lattice vector $\vec{c}_{11}^{(i)}$ was fixed at magnitudes increasing in 1 Å increments from $|\vec{c}_{11}^{(i)}| = 2 \text{ Å}, \dots, 16 \text{ Å}$ inclusive, to make a total of 15 unit cells. In all of these, the carbon layer was placed in the centre of the vacuum slab at fractional coordinate $0.5 \left| \vec{c}_{11}^{(i)} \right|$. A geometry optimisation calculation was carried out on each of these, in which the atomic positions and lengths $|\vec{a}_{11}^{(i)}|$ and $|\vec{b}_{11}^{(i)}|$ were relaxed, all unit cell angles were fixed, and $|\vec{c}_{11}^{(i)}|$ was fixed at the value appropriate to each case. The fully-optimised TS-corrected enthalpies were plotted against the vacuum thickness $|\vec{c}_{11}^{(i)}|$ to serve two purposes. Firstly, to identify the smallest value of $|\vec{c}_{11}^{(i)}|$ for which the undesired inter-cellular interlayer interaction in the vacuum direction had converged to zero. This value of $|\vec{c}_{11}^{(i)}|$ was named $|\vec{c}_{11}|$ and identified as $|\vec{c}_{11}| = 12 \text{ Å}$. Secondly, it served to calculate the carbon-carbon bond lengths as optimised using the particular

choice of functional, along with the corresponding optimised values of $|\vec{a}_{11}^{(i)}|$ and $|\vec{b}_{11}^{(i)}|$. These values were named $|\vec{a}_{11}|$ and $|\vec{b}_{11}|$ respectively, and recorded at values $|\vec{a}_{11}| = |\vec{b}_{11}| = 2.459 \text{ \AA}$ (4 s. f.). A similar procedure was then repeated for the case of 2 layer and 3 layer graphene on the multilayer unit cell shown in Figure 8 (b), in which the top carbon layer was placed at the centre of the vacuum similar to above. From similarly designed geometry optimisation calculations, the minimum required vacuum thicknesses for the 2 and 3 layer cases, $|\vec{c}_{21}|$ and $|\vec{c}_{31}|$, were identified as $|\vec{c}_{21}| = 16 \text{ \AA}$ and $|\vec{c}_{31}| = 20 \text{ \AA}$. The corresponding in-plane lattice parameters were found to be $|\vec{a}_{21}| = |\vec{b}_{21}| = 2.457 \text{ \AA}$ (4 s. f.) and $|\vec{a}_{31}| = |\vec{b}_{31}| = 2.456 \text{ \AA}$ (4 s. f.), and the corresponding optimised interlayer spacings were found to be $d_{s(21)} = 3.360 \text{ \AA}$ (4 s. f.) and $d_{s(31)} = 3.354 \text{ \AA}$ (4 s. f.).

Next, vacuum-filled cubic supercells were constructed containing a metal atom placed directly in the centre as shown in Figure 8 (c). Each supercell had lattice parameters fixed at values of $|\vec{A}_m| = |\vec{B}_m| = |\vec{C}_m|$ with $m = \text{Au, Al, Cr}$ as appropriate, with $|\vec{A}_m|$ increasing (along with $|\vec{B}_m|$ and $|\vec{C}_m|$) in 1 \AA increments from 2 \AA to 15 \AA inclusive, to make a total of $14 \times 3 = 42$ cubic supercells. TS-corrected zero point energy calculations were carried out for each, and the supercell energies were converged with respect to the supercell size in order to decouple the intercellular metal-metal interactions. The minimum supercell size required to satisfy the decoupling condition all metals was identified as $|\vec{A}_m| = |\vec{B}_m| = |\vec{C}_m| = 10 \text{ \AA}$.

The supercell shown in Figure 8 (d) was then constructed by forming a 2×2 array of the fully-optimised single graphene layer unit cells shown in Figure 8 (a). The supercell lattice vectors were fixed at values $\vec{A}_{11,m} = 2\vec{a}_{11}$ and $\vec{B}_{11,m} = 2\vec{b}_{11}$, and the vacuum-direction lattice parameter $\vec{C}_{11,m}^{(i)}$ was initially fixed at magnitudes increasing in 1 \AA increments from $|\vec{C}_{11,m}^{(i)}| = 6 \text{ \AA}, \dots, 27 \text{ \AA}$ inclusive, to make 22 supercells. Into each of these 22 supercells, a metal atom of species $m = \text{Au, Al, Cr}$ was placed 2 \AA directly above the central carbon atom as indicated in Figure 8 (d) by the red cross, thus creating a total of $22 \times 3 = 66$ supercells. In each one of these supercells, the carbon layer was fixed at the centre of the vacuum at fractional coordinate $0.5|\vec{C}_{11,m}^{(i)}|$. TS-corrected zero point energy calculations were carried out with the self-consistent electrostatic dipole correction scheme of Neugebauer & Scheffler⁵³ and the energy was plotted vs. $|\vec{C}_{11,m}^{(i)}|$ for each. This served the purpose of establishing the minimum vacuum thickness required to converge both intercellular interactions in the direction $\vec{C}_{11,m}^{(i)}$ and spurious intercellular dipole-dipole interactions to zero. The smallest value of $|\vec{C}_{11,m}^{(i)}|$ for which the energy plots were deemed to have converged for all metals was named $|\vec{C}_{11,m}|$ and identified as $|\vec{C}_{11,m}| = 20 \text{ \AA}$. A similar procedure was repeated for the 2 and 3 layer cases using the optimised interlayer spacings determined above. The top carbon layer was again fixed at the centre of the vacuum and the corresponding required vacuum thicknesses were found to be $|\vec{C}_{21,m}| = 24 \text{ \AA}$ and $|\vec{C}_{31,m}| = 27 \text{ \AA}$.

3 single layer supercells were constructed from 3×3 , 4×4 and 5×5 arrays of the fully relaxed unit cells from Figure 8 (a), whose vacuum-direction lattice vector \vec{C}_{11} fixed at the value $\vec{C}_{11} = 20 \text{ \AA}$ in all cases. This vacuum thickness was chosen so as to meet the requirements of the individual convergence tests just described; i.e. $|\vec{C}_{11}| = |\vec{C}_{11,m}| > |\vec{c}_{11}|$. A metal atom of species m was placed 2 \AA above the central carbon atom for each of these 3 supercells, with $m = \text{Au, Al}$ and Cr as appropriate, thereby producing a total of $3 \times 3 = 9$ supercells. TS-corrected zero-point energy calculations were carried out for these 9 systems and the total energy was plotted against supercell size for each metal to identify the minimum size required to decouple all intercellular adatom interactions. The 5×5 supercells with lattice parameters $|\vec{A}_{11}| = |\vec{B}_{11}| = 5|\vec{a}_{11}|$ were deemed sufficient for this purpose. It was also verified that this choice satisfied the intercellular metal-metal convergence requirement established above since $|\vec{A}_{11}| > |\vec{A}_m|$. No similar test of in-plane supercell sizes for multilayer + metal systems was carried out owing to the extensive computational cost involved. Supercell sizes of 5×5 unit cells were used for 2 and 3 layer cases, with $|\vec{A}_{21}| = |\vec{B}_{21}| = 5|\vec{a}_{21}|$ and $|\vec{C}_{21}| = 24 \text{ \AA}$ for the 2 layer system and $|\vec{A}_{31}| = |\vec{B}_{31}| = 5|\vec{a}_{31}|$ and $|\vec{C}_{31}| = 27 \text{ \AA}$ for the 3 layer system, with the top carbon layer once again placed in the centre of the vacuum. Measures taken to estimate the error in the calculated binding energies due to lattice perturbations under relaxation and the limited size of the 5×5 supercells are outlined in section II. B.

For the monolayer edge binding supercells, graphene edge slab/vacuum supercells akin to those shown in Figure 4 were prepared, in which metal atoms of species $m = \text{Au, Al, Cr}$ were placed initially at each end of the slab in the graphene plane as indicated by the red crosses at an initial distance of 2 \AA from the nearest C atom(s). For the zigzag edge slabs, a series of geometry optimisation calculations was carried out in order to converge the total relaxed TS-corrected system enthalpy with respect to the slab width $\vec{A}_{11,\text{zigzag}}$, and the slab thickness + vacuum thickness, whose sum is denoted $\vec{B}_{11,\text{zigzag}}$. The intercellular layer spacings were fixed at the

value $|\bar{C}_{11}| = 20 \text{ \AA}$, thus satisfying the test described earlier. The total binding energy was deemed to have converged for arrays of 5×8 of the appropriate unit cells for sites Z_1 and Z_2 . In an identical manner, an array of 5×7 appropriate unit cells for sites C_1 and C_2 was deemed sufficient. The vacuum thickness in both cases was set at 20 \AA . Example supercells are illustrated in Figure 4. Recent work has suggested possible reconstruction at graphene edges⁷⁵, however this extra detail was not deemed necessary for this work.

For all calculations in this section, the exit criterion was defined as a total change in system energy of $< 5 \times 10^{-3} \text{ eV}$ between successive calculations.

VI. REFERENCES

- ¹K. S. Novoselov, A. K. Geim, S.V. Morozov, D. Jiang, Y. Zhang, S.V. Dubonos, I. V. Grigorieva and A.A. Firsov *Science* **306**, 666 (2004)
- ²F. Schwierz *Nature Nanotechnology* **5**, 487 (2010)
- ³Y. Wu, V. Perebeinos, Y-M. Lin, T. Low, F. Xia and P. Avouris *Nano Letters* **12**, 1417 (2012)
- ⁴K. Nagashio, T. Nishimura, K. Kita and A. Toriumi *Japanese Journal of Applied Physics* **49**, 051304 (2010)
- ⁵K. Nagashio, T. Nishimura, K. Kita and A. Toriumi *Applied Physics Letters* **97**, 143514 (2010)
- ⁶S. Russo, M. F. Craciun, M. Yamamoto, A. F. Morpurgo and S. Tarucha *Physica E: Low-dimensional Systems and Nanostructures* **42**, 677 (2010)
- ⁷P. A. Khomyakov, A. A. Starikov, G. Brocks and P. J. Kelly *Physical Review B* **82**, 115437 (2010)
- ⁸R. S. Sundaram, M. Steiner, H-Y. Chiu, M. Engel, A. A. Bol, R. Krupke, M. Burghard, K. Kern and P. Avouris *Nano Letters* **11**, 3833 (2011)
- ⁹M. P. Lima, Antônio J. R. da Silva and A. Fazio *Physical Review B* **84**, 245411 (2011)
- ¹⁰J. Ding, Z Qiao, W. Feng, Y. Yao and Q. Niu *Physical Review B* **84**, 195444 (2011)
- ¹¹H. Valencia, A. Gil and G. Frapper *The Journal of Physical Chemistry C* **114**, 14141 (2010)
- ¹²R. Varns and P. Strange *Journal of Physics: Condensed Matter* **20**, 225005 (2008)
- ¹³M. Sargolzaei and F. Gudarzi *Journal of Applied Physics* **110**, 064303 (2011)
- ¹⁴K. Nakada and A. Ishii *Solid State Communications* **151**, 13 (2011)
- ¹⁵C. Cao, M. Wu, J. Jiang and H-P. Cheng *Physical Review B* **81**, 205424 (2010)
- ¹⁶A. Ishii, M. Yamamoto, H. Asano and K. Fujiwara *Journal of Physics: Conference Series* **100**, 052087 (2008)
- ¹⁷K.T. Chan, J. B. Neaton and M. L. Cohen *Physical Review B* **77**, 235430 (2008)
- ¹⁸M. Amft, S. Lebègue, O. Eriksson and N. V. Skorodumova *Journal of Physics: Condensed Matter* **23**, 395001 (2011)
- ¹⁹Z. M. Ao, Q. Jiang, R. Q. Zhang, T. T. Tan and S. Li *Journal of Applied Physics* **105**, 074307 (2009)
- ²⁰L. Hu, X. Hu, X. Wu, C. Du, Y. Dai and J. Deng *Physica B: Physics of Condensed Matter* **405**, 3337 (2010)
- ²¹H. Johll and H.C. Kang *Physical Review B* **79**, 245416 (2009)
- ²²Y. Mao, J. Yuan and J. Zhong *Journal of Physics: Condensed Matter* **20**, 115209 (2008)
- ²³O. V. Yazyev and A. Pasquarello *Physical Review B* **82**, 045407 (2010)
- ²⁴J. K-Hwan, C. S-Myeong and J. S-Hoon *Physical Review B* **82**, 033414 (2010)
- ²⁵Y. Tang, Z. Yang and Xianqi Dai *The Journal of Chemical Physics* **135**, 224704 (2011)
- ²⁶D. W. Boukhvalov and M. I. Katsnelson *Applied Physics Letters* **95**, 023109 (2009)
- ²⁷S. Malola, H. Hakkinen and P. Koskinen *Applied Physics Letters* **94**, 043106 (2009)
- ²⁸E. J. G. Santos, A. Ayuela and D. Sánchez-Portal *New Journal of Physics* **12**, 053012 (2010)
- ²⁹O. Cretu, A. V. Krasheninnikov, J. A. Rodríguez-Manzo, L. Sun, R. M. Nieminen and F. Banhart *Physical Review Letters* **105**, 196102 (2010)
- ³⁰E. J. G. Santos, D. Sánchez-Portal and A. Ayuela *Physical Review B* **81**, 125433 (2010)
- ³¹S. Karoui, H. Amara, C. Bichara and F. Ducastelle *ACS Nano* **4**, 6114 (2010)
- ³²R. Zan, Q. M. Ramasse, U. Bangert, K. S. Novoselov *Nano Letters* **12**, 3936 (2012)
- ³³R. Zan, U. Bangert, Q. M. Ramasse and K. S. Novoselov *Nano Letters* **11**, 1087 (2011)
- ³⁴R. Zan, U. Bangert, Q. M. Ramasse and K. S. Novoselov *Small* **7**, 2868 (2011)
- ³⁵Q. M. Ramasse, R. Zan, U. Bangert, D.W. Boukhvalov, Y-W. Son and K. S. Novoselov *ACS Nano* **6**, 4063 (2012)
- ³⁶J. P. Perdew, K. Burke and M. Ernzerhof *Physical Review Letters* **77**, 3865 (1996)
- ³⁷S. Grimme *Journal of Computational Chemistry* **27**, 1787 (2006)
- ³⁸H. Rydberg, M. Dion, N. Jacobson, E. Schröder, P. Hyldgaard, S. Simak, D. Langreth and B. Lundqvist *Physical Review Letters* **91**, 126402 (2003)
- ³⁹M. Dion, H. Rydberg, E. Schröder, D. Langreth and B. Lundqvist *Physical Review Letters* **92**, 246401 (2004)
- ⁴⁰M. Dion, H. Rhydberg, E. Schröder D. Langreth and B. Lundqvist *Physical Review Letters* **95**, 109902 (2005)
- ⁴¹P. Jurečka, J. Černý, P. Hobza and D. R. Salahub *Journal of Computational Chemistry* **28**, 555 (2007)
- ⁴²A. Tkatchenko and M. Scheffler *Physical Review Letters* **102**, 073005 (2009)
- ⁴³L. G. De Arco, Y. Zhang, A. Kumar, and C. Zhou *IEEE Transactions on Nanotechnology* **8**, 135 (2009)

- ⁴⁴D. Wei, Y. Liu, H. Zhang, L. Huang, B. Wu, J. Chen and G. Yu *Journal of the American Chemical Society* **131**, 11147 (2009)
- ⁴⁵A. Malesevic, R. Vitchev, K. Schouteden, A. Volodin, L. Zhang, G. Van Tendeloo, A. Vanhulsel and C. Van Haesendonck *Nanotechnology* **19**, 305604 (2008)
- ⁴⁶A. Reina, X. Jia, J. Ho, D. Nezich, H. Son, V. Bulovic, M. S. Dresselhaus and J. Kong *Nano Letters* **9**, 30 (2009)
- ⁴⁷G. Ming, J. J. Belbruno, S. D. Kenny and R. Smith *Surface Science* **541**, 91 (2003)
- ⁴⁸T. Eberlein, U. Bangert, R. R. Nair, R. Jones, M. Gass, A. L. Bleloch, K. S. Novoselov, A. Geim and P. R. Briddon *Physical Review B* **77**, 233406 (2008)
- ⁴⁹J. C. Meyer, A. K. Geim, M. I. Katsnelson, K. S. Novoselov, T. J. Booth and S. Roth *Nature* **446**, 60 (2007)
- ⁵⁰A. Fasolino, J. H. Los and M. I. Katsnelson *Nature Materials* **6**, 858 (2007)
- ⁵¹P. Lambin, H. Amara, F. Ducastelle and L. Henrard *Physical Review B* **86**, 045448 (2012)
- ⁵²G. Makov and M. C. Payne *Physical Review B* **51**, 4014 (1995)
- ⁵³J. Neugebauer and M. Scheffler *Physical Review B* **46**, 16067 (1992)
- ⁵⁴L. Bengtsson *Physical Review B* **59**, 12301 (1999)
- ⁵⁵L. N. Kantorovich *Physical Review B* **60**, 15476 (1999)
- ⁵⁶P. Schultz *Physical Review B* **60**, 1551 (1999)
- ⁵⁷I.-C. Yeh and M. L. Berkowitz *Journal of Chemical Physics* **111**, 3155 (1999)
- ⁵⁸T. M. Nymand and P. Linse *Journal of Chemical Physics* **112**, 6152 (2000)
- ⁵⁹I. Hamada, M. Otani, O. Sugino and Y. Morikawa *Physical Review B* **80**, 165411 (2009)
- ⁶⁰S. J. Clark, M. D. Segall, C. J. Pickard, P. J. Hasnip, M. J. Probert, K. Refson and M. C. Payne *Zeitschrift fuer Kristallographie* **220**, 567 (2005)
- ⁶¹D. Vanderbilt *Physical Review B* **41**, 7892 (1990)
- ⁶²E. R. McNellis, J. Meyer, and K. Reuter *Physical Review B* **80**, 205414 (2009)
- ⁶³P. Trucano and R. Chen *Journal of the Chemical Society, Faraday Transactions 2: Molecular and Chemical Physics* **72**, 446 (1976)
- ⁶⁴H. J. Monkhorst and J. D. Pack *Physical Review B* **13**, 5188 (1976)
- ⁶⁵C. G. Broyden *IMA Journal of Applied Mathematics* **6**, 76 (1970)
- ⁶⁶C. G. Broyden *IMA Journal of Applied Mathematics* **6**, 222 (1970)
- ⁶⁷R. Fletcher *The Computer Journal* **13**, 317 (1970)
- ⁶⁸D. Goldfarb *Mathematics of Computation* **24**, 23 (1970)
- ⁶⁹D. F. Shanno *Mathematics of Computation* **24**, 647 (1970)
- ⁷⁰T. A. Halgren and W. N. Lipscomb *Chemical Physics Letters*, **49** 225 (1977)
- ⁷¹N. Govind, M. Peterson, G. Fitzgerald, D. K-Smith and J. Andzelm *Computational Materials Science* **28**, 250 (2003)
- ⁷²H. Wang, K. Li, Y. Cheng, Q. Wang, Y. Yao, U. Schwingenschlöggl, X. Zhang and W. Yang *Nanoscale* **4**, 2920 (2012)
- ⁷³J. C. Meyer, F. Eder, S. Kurasch, V. Skakalova, J. Kotakoski, H. J. Park, S. Roth, A. Chuvilin, S. Eyhusen, G. Benner, A. V. Krashennnikov and U. Kaiser *Physical Review Letters* **108**, 196102 (2012)
- ⁷⁴R. F. Egerton, P. Li and M. Malac *Micron* **35**, 399 (2004)
- ⁷⁵P. Koskinen, S. Malola and H. Häkkinen *Physical Review Letters* **101**, 115502 (2008)

VII. ACKNOWLEDGEMENTS

T. P. H. would like to thank the UK EPSRC for the Doctoral Training Award which funded this research. We acknowledge use of Hartree Centre resources in this work. The STFC Hartree Centre is a research collaboration in association with IBM providing High Performance Computing platforms funded by the UK's investment in e-Infrastructure. The Centre aims to develop and demonstrate next generation software, optimised to take advantage of the move towards exa-scale computing. Additional high performance computing facilities were provided by the ARC1 resource at the University of Leeds. SuperSTEM is the UK EPSRC National Facility for Aberration-Corrected Scanning Transmission Electron Microscopy.

VIII. FIGURES AND CAPTIONS

Binding energy, E_b , of Au adatom on pristine single layer graphene / eV. All values quoted to 3 d.p. unless otherwise specified									
<i>XC Functional</i>	<i>LDA</i>			<i>GGA PBE</i>			<i>GGA PBE van der Waals-corrected {correction scheme used}</i>		
Author	Atop (A)	Bridge (B)	Hollow (H)	Atop (A)	Bridge (B)	Hollow (H)	Atop (A)	Bridge (B)	Hollow (H)
⁹ Lima	-	-	-	-0.410	-	-	-	-	-
²⁵ Tang	-	-	-	-0.075	-	-	-	-	-
¹⁰ Ding	-0.77(2d.p.)	-	-0.50(2d.p.)	-0.16(2d.p.)	-	-0.16(2d.p.)	-	-	-
¹² Varns & Strange	-0.79(2d.p.)	-0.74(2d.p.)	-0.52(2d.p.)	-	-	-	-	-	-
¹⁷ Chan	-	-	-	-0.096	-0.089	-0.085	-	-	-
¹⁸ Amft	-0.732	-0.698	-0.451	-0.099	-0.081	no bond	-0.385 {Dion et al. ³⁸⁻⁴⁰ -0.886 {Grimme ³⁷ }	-0.314 {Dion et al. ³⁸⁻⁴⁰ -0.881 {Grimme ³⁷ }	-0.322 {Dion et al. ³⁸⁻⁴⁰ -0.870 {Grimme ³⁷ }

Table 1. Recently published DFT-calculated Au adatom/graphene binding energies on the 3 high symmetry adsorption sites of single layer graphene. Negative binding energies signify that the configurations are stable, as per equation (1.1).

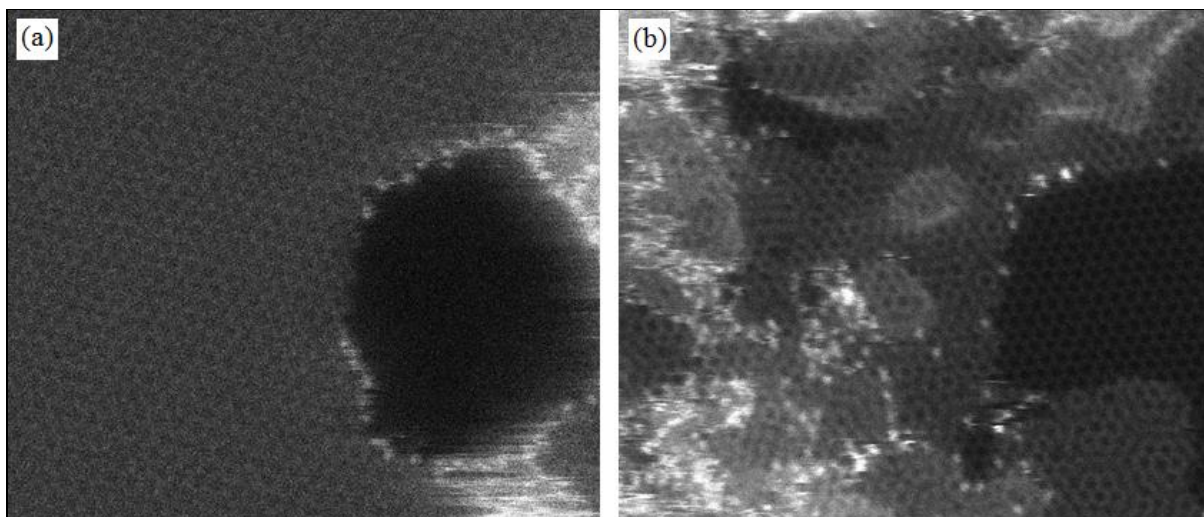
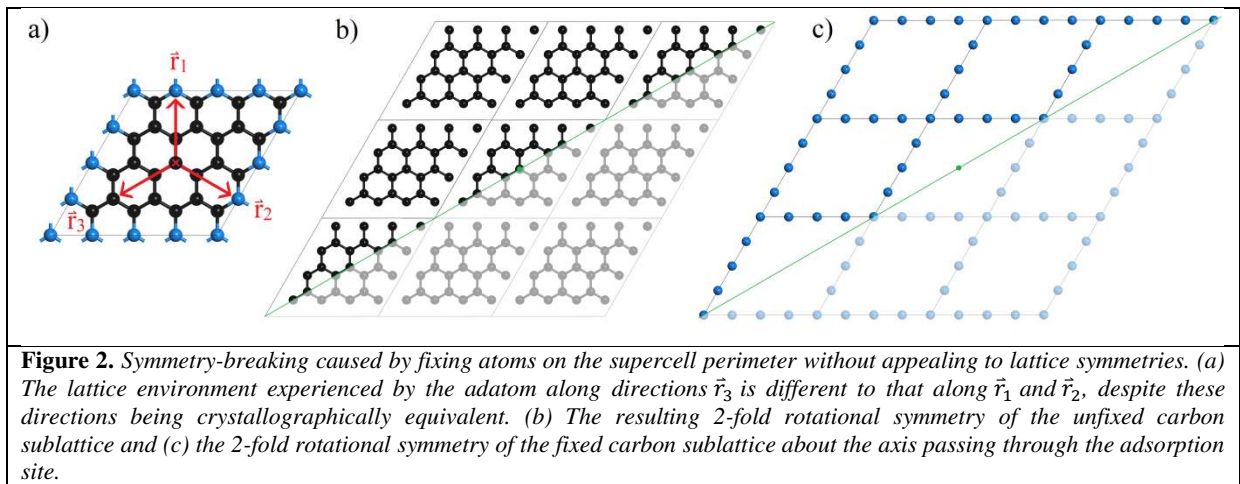


Figure 1. STEM HAADF images at 60 keV showing preferential binding of metal atoms to edge defects, hydrocarbon-contaminated regions and metal clusters. (a) Monolayer graphene sheet with hole, onto which a 2Å layer of Al was evaporated. Al atoms are seen only at edge sites and in clusters near the hole³⁵. (b) Monolayer graphene sheet with bilayer and trilayer regions onto which a 5Å layer of Au gold was evaporated. Individual Au atoms and Si contaminants (of less bright contrast) clearly bind preferentially to edge sites. The pristine regions of the lattice are completely devoid of adatoms in both cases.



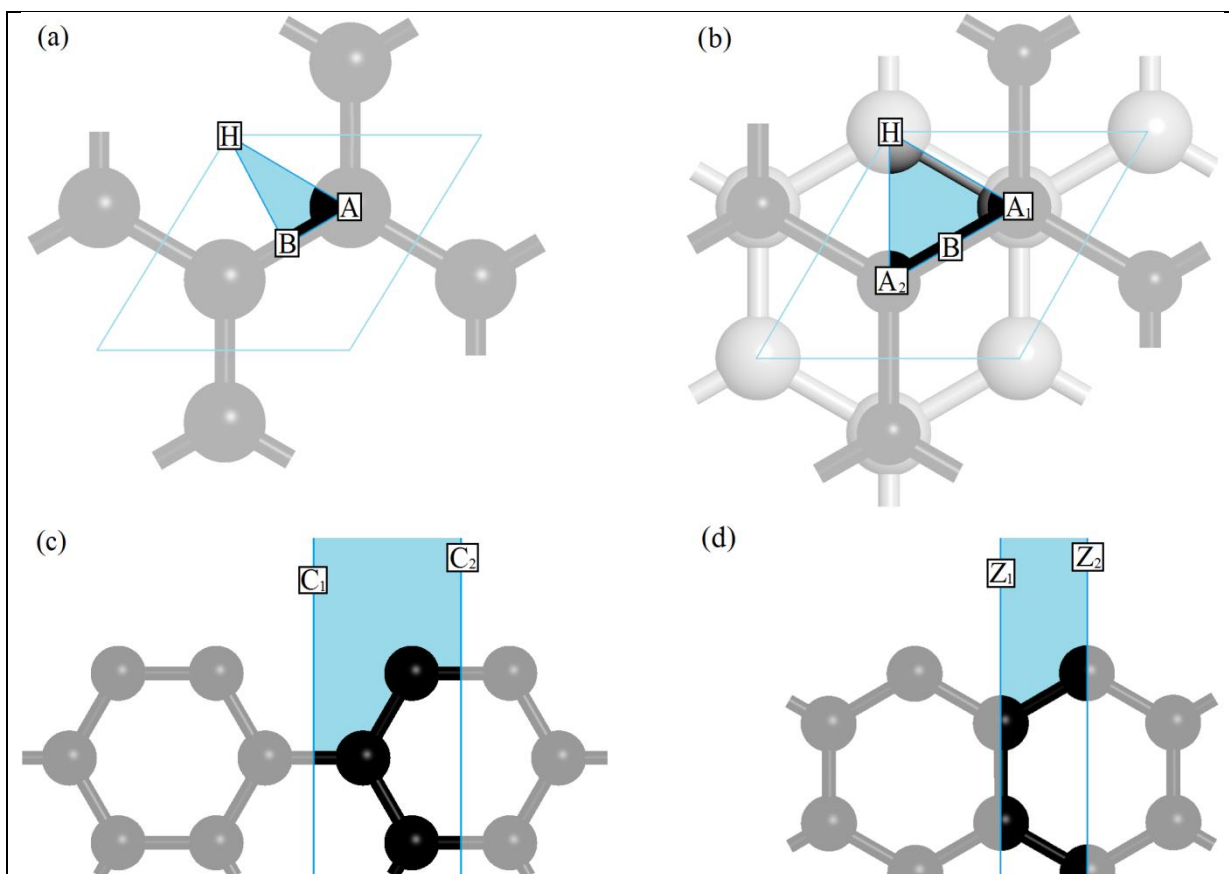
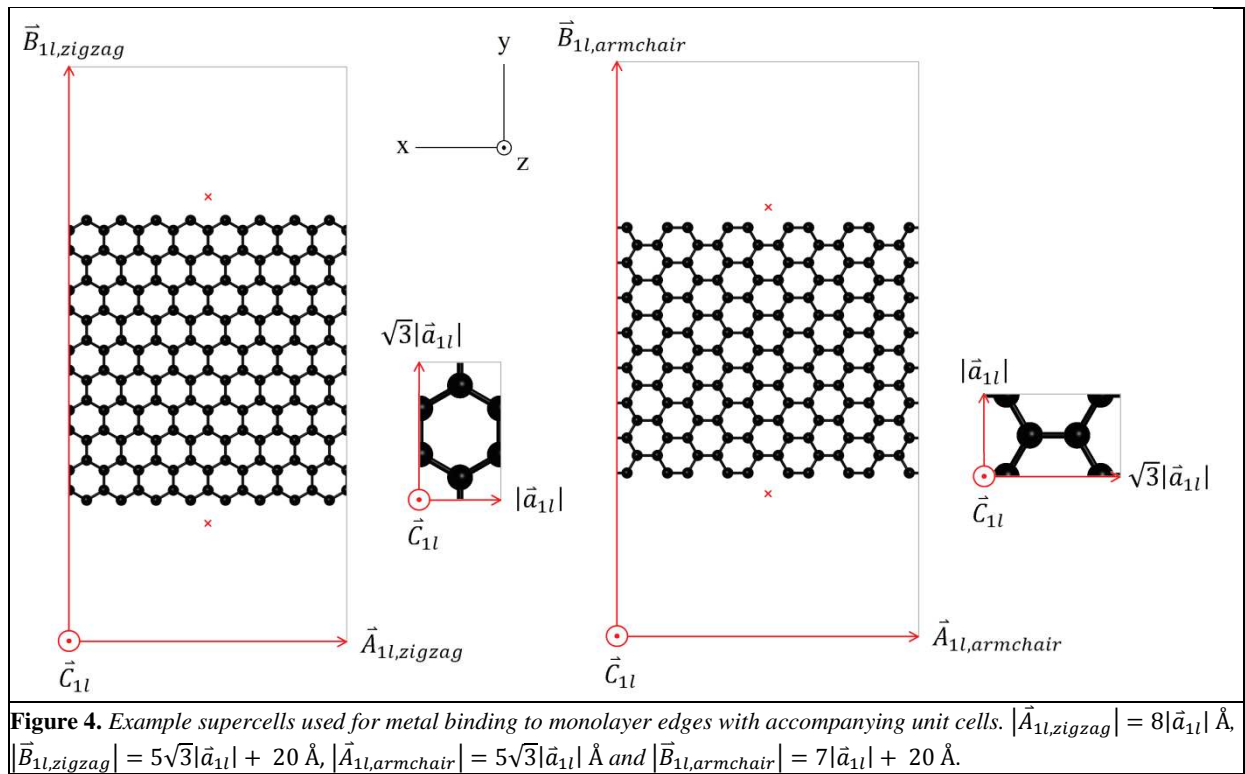


Figure 3. The high symmetry adsorption sites located at the vertices of the symmetry-reduced Wigner Seitz cell boundaries for (a) single layer graphene and (b) 2+ layer graphene, for which AB stacking is assumed. In the multilayer case, the top layer is represented by small black balls and sticks and the sublayer is represented by large grey balls and sticks. (c) & (d) The high symmetry binding sites of the monolayer armchair edge and zigzag edge considered in this work.



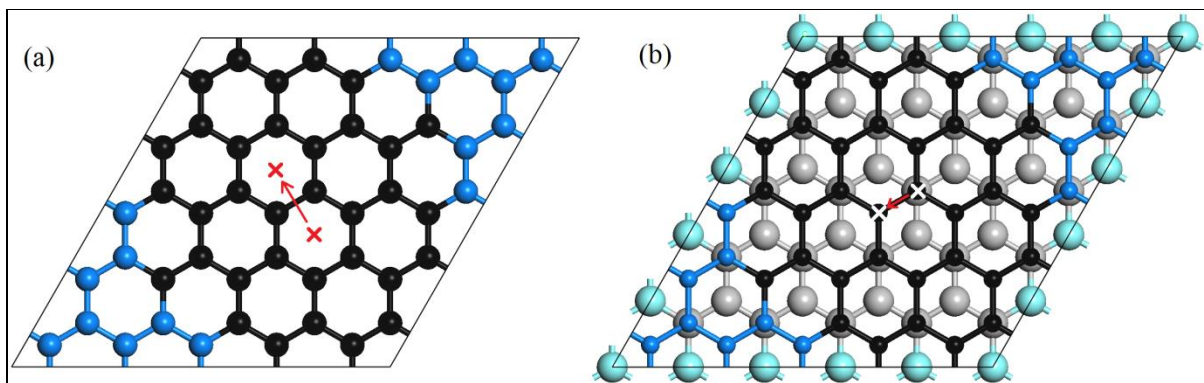
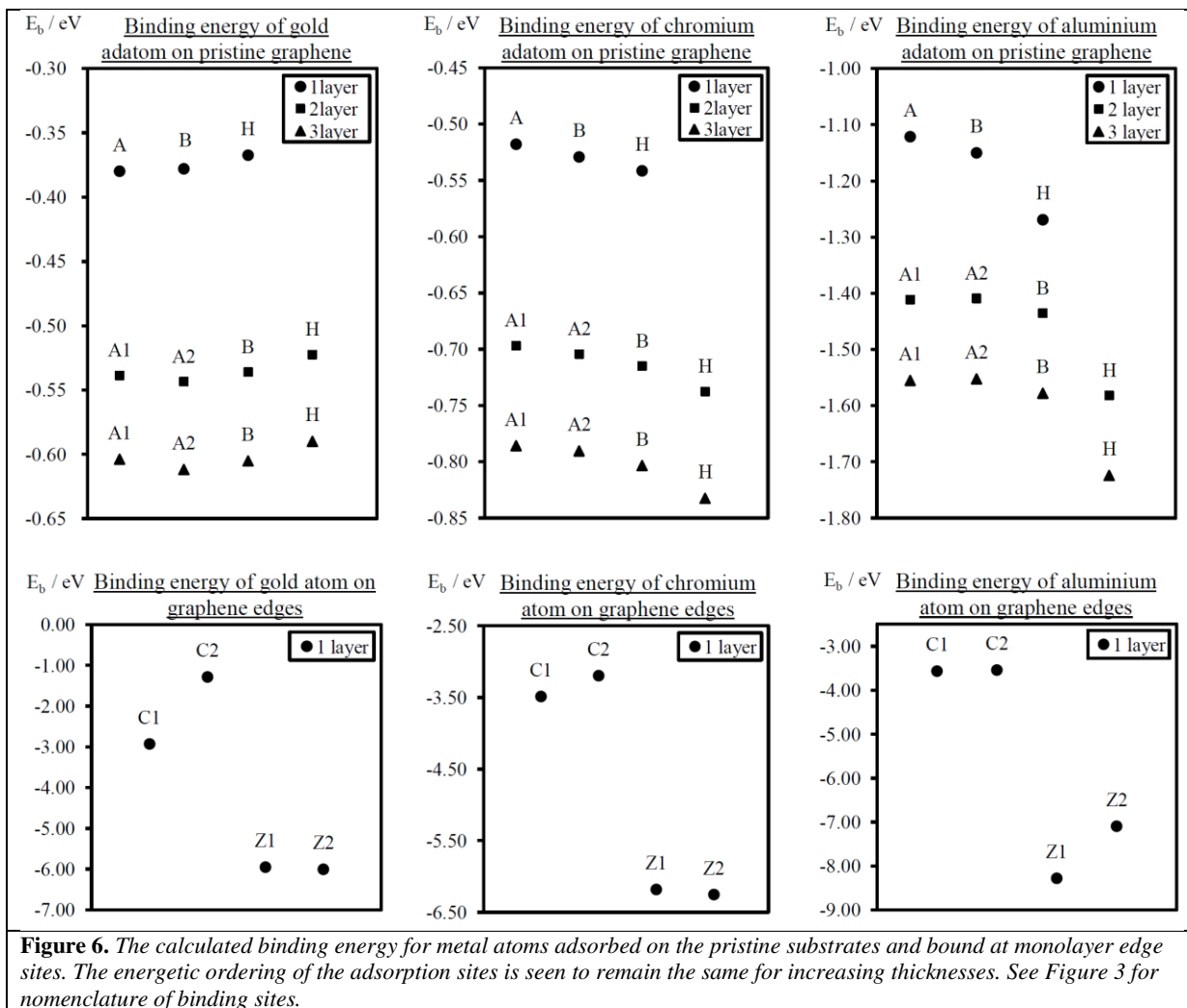


Figure 5. Example supercells used for migration activation barrier calculations. (a) $H \rightarrow B \rightarrow H$ trajectory used for Cr and Al on the monolayer (b) $A_1 \rightarrow B \rightarrow A_2$ trajectory used for Au.



Metal / graphene system	Site	Binding energy, E_b / eV (3 d.p.)	Distance from metal (ad)atom to nearest carbon atom(s) along bond direction(s) / Å (3 d. p.)	Distance along z axis from metal adatom to nearest carbon atom(s) / Å (3 d. p.)	Distance along z axis from metal adatom to fixed top layer carbon atoms / Å (3 d. p.)
Au					
1 layer adsorption sites	A	-0.380	3.082	3.082	3.095
	B	-0.378	3.291	3.215	3.217
	H	-0.367	3.700	3.421	3.408
2 layer adsorption sites	A ₁	-0.539	3.008	3.008	3.025
	A ₂	-0.543	2.661	2.661	2.731
	B	-0.536	3.283	3.207	3.209
3 layer adsorption sites	H	-0.522	3.665	3.383	3.379
	A ₁	-0.604	2.729	2.729	2.807
	A ₂	-0.612	2.702	2.702	2.765
1 layer edge sites	B	-0.605	3.233	3.156	3.159
	H	-0.590	3.650	3.366	3.360
	C ₁	-2.927	2.125	-	-
1 layer edge sites	C ₂	-1.284	2.154	-	-
	Z ₁	-5.950	2.171	-	-
	Z ₂	-6.003	2.004	-	-
Cr					
1 layer adsorption sites	A	-0.518	2.299	2.299	2.322
	B	-0.529	2.359	2.250	2.264
	H	-0.542	2.499	2.056	2.063
2 layer adsorption sites	A ₁	-0.697	2.295	2.295	2.308
	A ₂	-0.704	2.288	2.288	2.299
	B	-0.715	2.356	2.247	2.254
3 layer adsorption sites	H	-0.738	2.493	2.049	2.048
	A ₁	-0.786	2.284	2.284	2.300
	A ₂	-0.790	2.279	2.279	2.291
1 layer edge sites	B	-0.803	2.344	2.231	2.243
	H	-0.832	2.473	2.025	2.020
	C ₁	-3.485	2.036	-	-
1 layer edge sites	C ₂	-3.090	1.942	-	-
	Z ₁	-6.181	1.827	-	-
	Z ₂	-6.252	1.893	-	-
Al					
1 layer adsorption sites	A	-1.121	2.277	2.277	2.241
	B	-1.150	2.347	2.236	2.235
	H	-1.269	2.563	2.127	2.135
2 layer adsorption sites	A ₁	-1.411	2.270	2.270	2.220
	A ₂	-1.409	2.272	2.272	2.230
	B	-1.435	2.349	2.239	2.215
3 layer adsorption sites	H	-1.582	2.568	2.135	2.133
	A ₁	-1.555	2.271	2.271	2.222
	A ₂	-1.552	2.272	2.272	2.212
1 layer edge sites	B	-1.578	2.349	2.240	2.216
	H	-1.724	2.570	2.137	2.133
	C ₁	-3.564	2.002	-	-
1 layer edge sites	C ₂	-3.539	1.892	-	-
	Z ₁	-8.280	1.976	-	-
	Z ₂	-7.095	1.935	-	-

Table 2. (Ad)atom binding energies metal-carbon distances associated with the fully relaxed structures. The differences between values in the two rightmost columns indicate the graphene lattice puckering distance in each adsorption case. Distances which are identical by definition are highlighted in grey pairs. See Figure 3 for nomenclature of binding sites.

Adatom	Substrate	Path	Migration barrier ΔE / eV (3.d.p.)
Au	1 layer	A \rightarrow B \rightarrow A	0.007
	2 layer	A ₁ \rightarrow B \rightarrow A ₂	0.008
		A ₂ \rightarrow B \rightarrow A ₁	0.024
	3 layer	A ₁ \rightarrow B \rightarrow A ₂	0.019
		A ₂ \rightarrow B \rightarrow A ₁	0.025
Cr	1 layer	H \rightarrow B \rightarrow H	0.022
	2 layer	H \rightarrow B \rightarrow H	0.021
	3 layer	H \rightarrow B \rightarrow H	0.022
Al	1 layer	H \rightarrow B \rightarrow H	0.166
	2 layer	H \rightarrow B \rightarrow H	0.178
	3 layer	H \rightarrow B \rightarrow H	0.197

Table 3. Calculated migration barriers for Au, Cr and Al on the lowest energy migration pathways on pristine monolayer, bilayer and trilayer graphene.

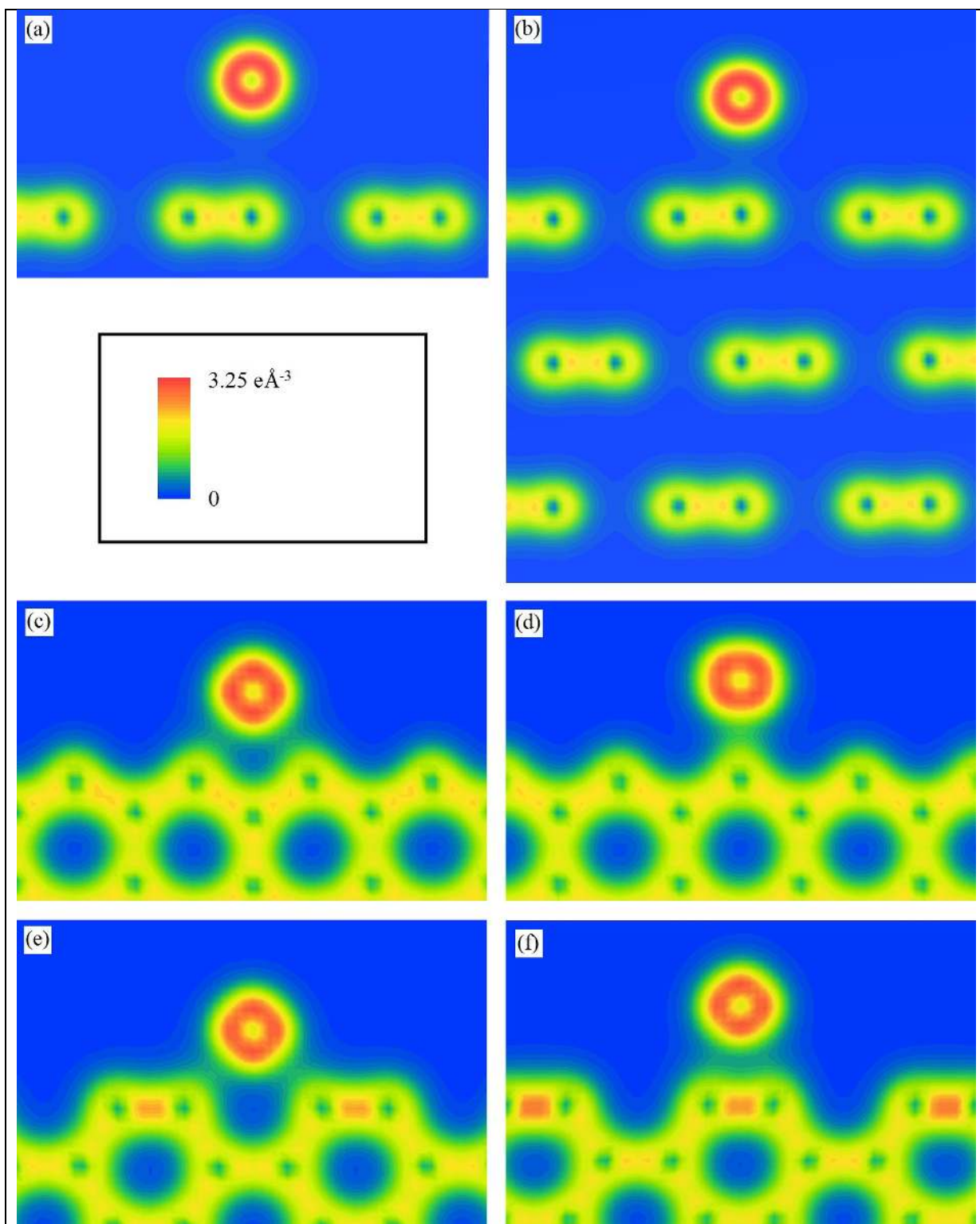


Figure 7. Electron density images showing the difference in bonding character between adsorption and edge sites for Au. (a) Cross section of the total electron density field shown in colour units of electrons / \AA^3 for Au at adsorption site A for the fully relaxed monolayer. (b) Corresponding trilayer image, showing Au at site A_1 . The cross sections shown intersect the graphene along the “armchair” direction, thus showing the carbon-carbon bonds for comparison. The bonding character is seen to be consistent with physisorption in both cases, though a slightly more substantial bond is evident for the trilayer case. Au atom binding to the edge sites (c) Z_1 (d) Z_2 (e) C_1 and (f) C_2 . Clear and substantial regions of electron density are observable in all four cases, consistent with a covalent metal carbide bond. See Figure 3 for nomenclature of binding sites.

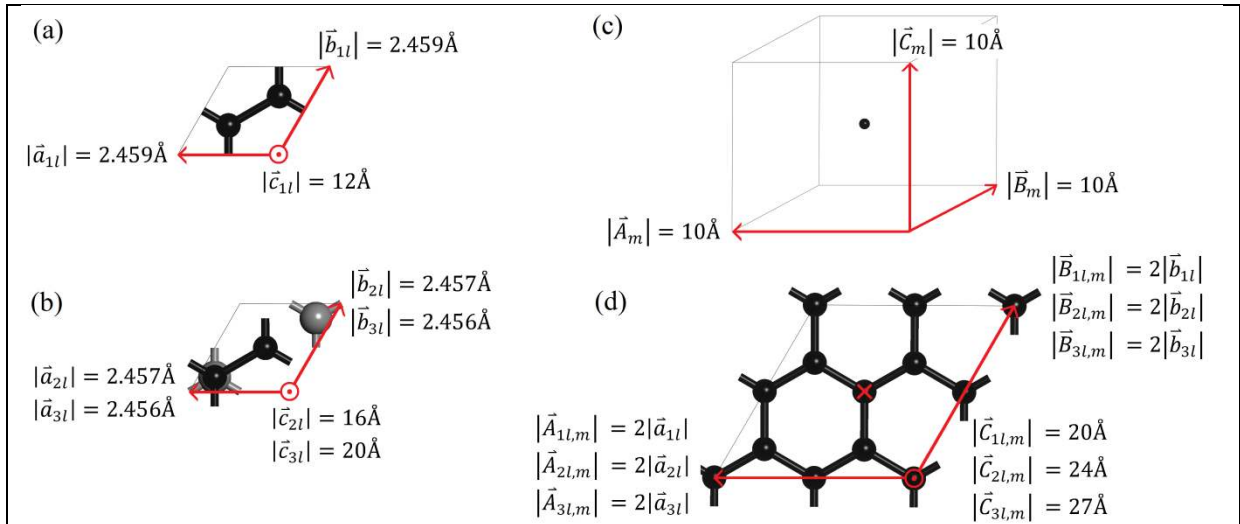


Figure 8. (a) Fully optimised graphene unit cell with relaxed lattice parameters in red. Atoms and bonds are represented by balls and sticks respectively. (b) Fully optimised multilayer graphene unit cell, as in (a). To aid visualisation, the atoms and bonds of the first sublayer are represented with large grey balls and sticks, and those of the top layer with small black balls and sticks. The second sublayer is not indicated owing to the assumed AB stacking structure (c) Isolated metal atom cubic supercell. The lattice parameters shown indicate the smallest supercell size required to decouple all intercellular metal-metal interactions (d) Graphene + metal supercell spanning 2×2 unit cells. The lattice parameters shown indicate the vacuum thicknesses required to decouple intercellular interactions along the vacuum direction only.

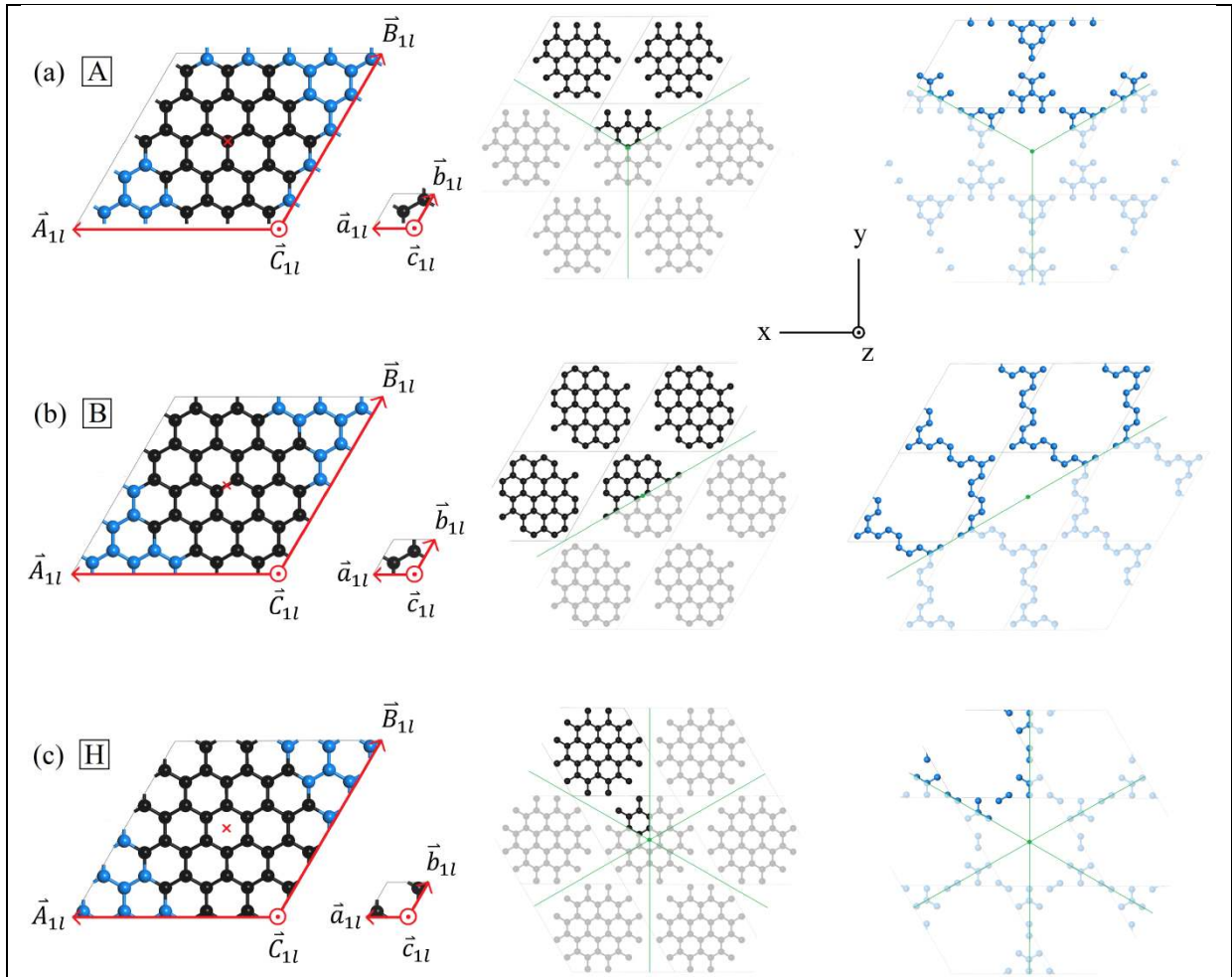


Figure 9. The 3 single layer supercells before geometry optimisation used for the adatom + graphene systems for (a) site A, (b) site B and (c) site H. In all cases, carbon atoms whose positions are fixed are represented in blue and those whose positions are relaxed are represented in black. The corresponding unfixed and fixed sublattices are displayed below, in which the green lines show boundaries between segments of the lattice which are equivalent by virtue of rotational symmetry about the axis passing through the adsorption site represented by the green dot in the centre. The red cross denotes the initial adatom location. $|\vec{a}_{1l}| = |\vec{b}_{1l}| = 2.459 \text{ \AA}$ (3 d. p.), $|\vec{A}_{1l}| = |\vec{B}_{1l}| = 5|\vec{a}_{1l}| = 12.29 \text{ \AA}$ (3 d. p.) and $|\vec{C}_{1l}| = |\vec{c}_{1l}| = 20 \text{ \AA}$. See Figure 3(main text) for nomenclature on adsorption sites.

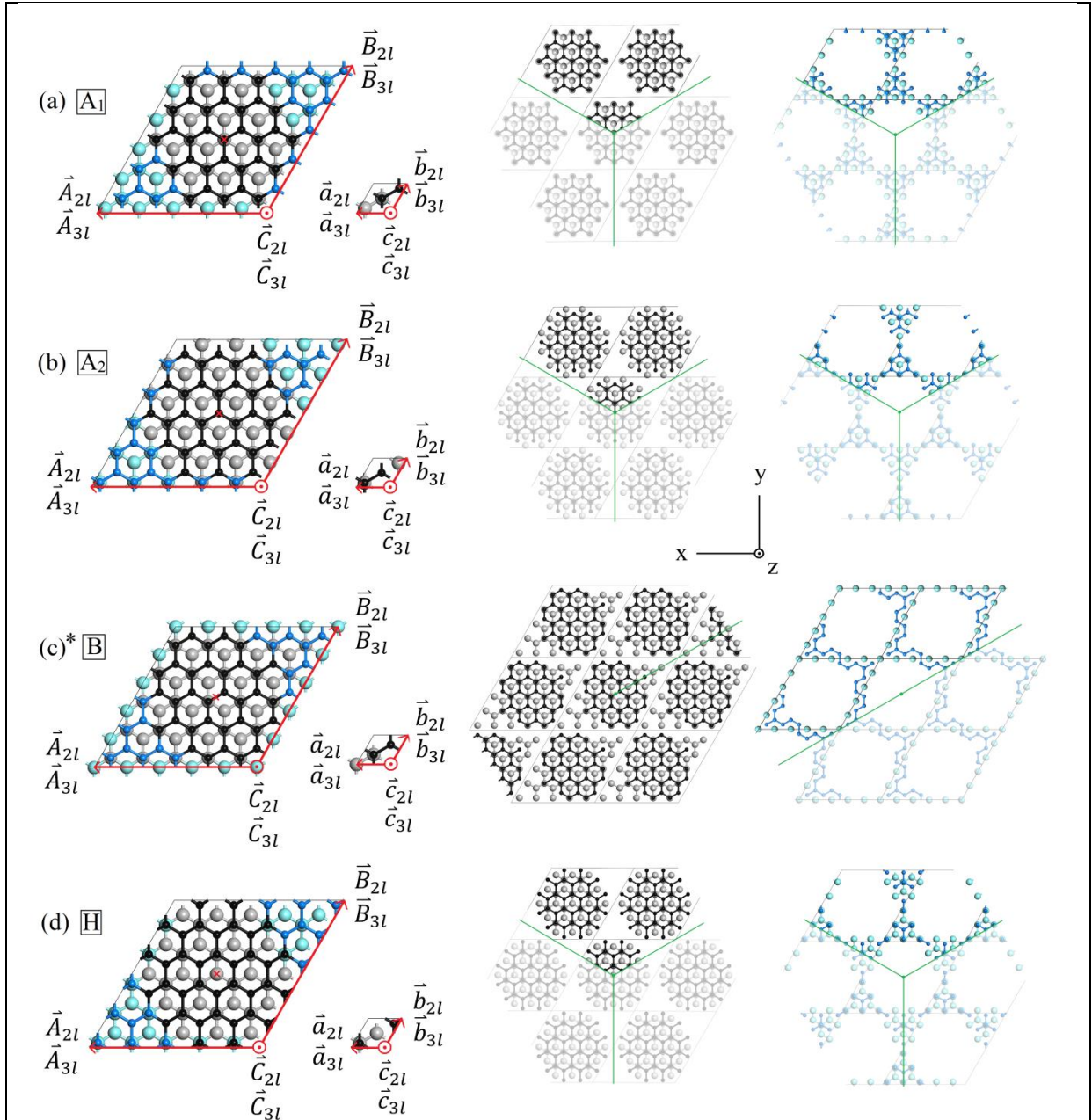


Figure 10. The multilayer input supercells for (a) site A_1 , (b) site A_2 (c) site B , and (d) site H . The top carbon layer is represented by small balls and sticks, and the first sublayer is represented by large balls and sticks. No further sublayers are indicated owing to the assumed AB stacking structure. Fixed top layer and sublayer C atoms are blue and light green respectively. Unfixed top layer and sublayer C atoms are coloured black and grey respectively. As in Figure 9, the red cross denotes the initial adatom location. As in Figure 9, the unfixed and fixed sublattices are shown below their corresponding supercell, divided into segments which are equivalent by rotational symmetry about the axis passing through the adsorption site. $|\vec{a}_{21}| = |\vec{b}_{21}| = 2.457 \text{ \AA}$ (3 d. p.), $|\vec{A}_{21}| = |\vec{B}_{21}| = 5|\vec{a}_{21}| = 12.28 \text{ \AA}$ (3 d. p.), $|\vec{C}_{21}| = |\vec{c}_{21}| = 24 \text{ \AA}$, $|\vec{a}_{31}| = |\vec{b}_{31}| = 2.456 \text{ \AA}$ (3 d. p.), $|\vec{A}_{31}| = |\vec{B}_{31}| = 5|\vec{a}_{31}| = 12.28 \text{ \AA}$ (3 d. p.) and $|\vec{C}_{31}| = |\vec{c}_{31}| = 27 \text{ \AA}$.

*The B site in (c) is the only site for which the rotational symmetry of the first sublayer (and also therefore the complete lattice) is 1-fold. For this case, C positions were fixed on the supercell perimeter on the first sublayer in preference to some other arbitrary selection resulting in 1-fold symmetry, resulting in the 2-fold fixed sublattice rotational symmetry shown. See Figure 3 (main text) for nomenclature on adsorption sites.